

Varied Competition among Three Multiferroic Phases of NiI₂ from the Bulk to the Monolayer Limit

Nanshu Liu¹, Cong Wang¹, Changlin Yan¹, Jun Hu^{2*}, Yanning Zhang^{3*}, Wei Ji^{1*}

¹*Beijing Key Laboratory of Optoelectronic Functional Materials & Micro-Nano Devices,
Department of Physics,
Renmin University of China, Beijing 100872, China*

²*School of Physical Science and Technology, Ningbo University, Ningbo, 315211, China*

³*Institute of Fundamental and Frontier Sciences, University of Electronic Science and Technology
of China, Chengdu, 610054, China*

Abstract:

The monolayer of NiI₂ was recently suggested to be a type-II multiferroic material, based on a presumed magnetic configuration and a supposed origin of the enhanced second harmonic generation (SHG) signal. Here, we found that such an assumption is flawed at the monolayer limit where a freestanding ML NiI₂ showing broken C_3 symmetry prefers to a striped antiferromagnetic order (AABB-AFM) along with an intralayer antiferroelectric (AFE) order. However, the C_3 symmetry of the monolayer may preserve under a substrate confinement, which leads to a spiral magnetic order (Spiral-Y), different from that of the bulk counterpart (Spiral-B). The Spiral-Y order persists up to 4L thickness and shows ferroelectricity (FE) ascribed to an inversed Dzyaloshinskii-Moriya (D-M) interaction. Thus, those three type-II multiferroic phases, namely Spiral-B+FE, Spiral-Y+FE and AABB-AFM+AFE, emerge for NiI₂ with different layer numbers and structural symmetries. Such a magnetic groundstate variation from the bulk to monolayer NiI₂ originates from the competition among thickness dependent D-M, Kitaev and Heisenberg spin-exchange interactions, as well as single-ion magnetic anisotropy. These theoretical results not only clarify the multiferroics of NiI₂, but also enlighten us the role of layer-stacking induced change of noncollinear spin-exchange interactions and magnetic anisotropy in thickness-dependent magnetic transitions of two-dimensional magnets.

*Corresponding authors. E-mail: hujun2@nbu.edu.cn; yanningz@uestc.edu.cn; wji@ruc.edu.cn.

Keywords: NiI₂, multiferroics, antiferromagnetism, spiral magnetism, magnetic anisotropic energy

Magnetoelectric (ME) effect, i.e., controlling magnetic (electric) properties by means of an electric (magnetic) field, has driven significant research interests in both fundamental physics and potential spintronic applications [1,2]. Multiferroic materials with consisting of magnetic and electric orders are thus ideal systems to obtain sufficient ME effect [3]. Among them, type-II multiferroics provide more possibilities to regulate electric polarization induced by a magnetic order spontaneously lacking inversion symmetry through the inversed Dzyaloshinskii-Moriya (D-M) interaction [4-7]. However, identification of type-II multiferroics in atomically thin van der Waals (vdW) form is still under debate.

Among one of the popular multiferroic materials, bulk NiI₂ has stimulated a surge of interest due to its rich temperature-dependent magnetic transition [8,9]. It undergoes two successive magnetic phase transitions from a para-magnetic (PM) to a interlayer anti-ferromagnetic (AFM) phase at $T_{N1} = 76$ K and then to a spiral magnetic phase below $T_{N2} = 59.5$ K [8]. The AFM to spiral transition accompanies with both rotational symmetry and inversion symmetry breakings, which induces an electric polarization through inversed D-M interaction, as reflected in second harmonic generation (SHG) [10] and birefringence signals [11].

Monolayer (ML) NiI₂ on a hBN substrate was recently evidenced to show multiferroicity (MF) under 20 K by an enhanced SHG signal [11]. The enhanced SHG signal is, in principle, ascribed to a broken inversion symmetry, which could be induced by either a magnetic or a geometric (electrical) origin. The magnetic state of ML NiI₂ under 20 K is still an open issue that no direct measurement is successfully conducted so far and previous density functional theory calculations predict the ferromagnetic (FM) [12-14] or AFM [15] groundstate for ML NiI₂. Although not conclusive, they are indeed different from the bulk groundstate. If the enhanced SHG signal originates from the

magnetic contribution, the SHG results for the NiI₂ monolayer thus cannot guarantee that additional electrical polarization forms under 20 K. Another measurement of ML NiI₂ on a SiO₂ substrate seconds this concern of the claimed MF monolayer [10] where no SHG enhancement is observable in the ML. Therefore, the statement of ML NiI₂ being an MF monolayer needs further verification beyond the SHG measurement, which is towards an interesting question whether the type-II multiferroicity could retain at the monolayer limit.

In this Letter, we studied the evolution of the magnetic groundstate and electrical polarization from the NiI₂ bulk to the ML using density functional theory (DFT) calculations. A tentative layer-dependent magnetic phase diagram was suggested, which manifests competitions among three magnetic phases while two (one) of them are (anti-) ferroelectric. The magnetic groundstate of the ML depends on the in-plane geometry distortion induced by the substrate. If the original C_3 structural symmetry is preserved by the substrate, the NiI₂ monolayer is a type-II MF layer showing a spiral (q_Y) magnetic order different from that of the bulk (q_B), which induces an in-plane electric polarization through the inverted D-M interaction. The D-M and Kitaev interactions, and Heisenberg spin-exchange interactions are involved in these competitions. Moreover, we constructed a NiI₂/hBN heterostructure most likely observed in the experiment, which helps explain the SHG signal of monolayer NiI₂ observed over 20 K. Our theoretical results explain the two pioneering experiments [10,11] for ML NiI₂ in a consistent way. In short, the NiI₂ monolayer is a 2D MF material at the monolayer limit, but with tunable multiferroicity, which highlights, again, the importance of thickness-dependence and in-plane geometry modulation for magnetic and related properties of 2D materials.

Our DFT calculations were performed using the Vienna ab initio Package (VASP) within the generalized gradient approximation (GGA) for the exchange correlation functional [16]. A kinetic energy cutoff for the plane-waves was set to 700 eV for structural optimization and 650 eV for energy and electronic properties calculations. Dispersion correction was performed at the Grimme's semiempirical D3 scheme [17]

to describe the vdW interaction between NiI₂ layers. K-meshes of 6×4×1, 13×7×1, 7×7×1, 5×5×1, 5×7×1, and 3×13×1 were used to sample the first Brillouin zone of 2×2√3×1, 1×√3×1, √3×√3×1, 3×3×1, 3×2×1, and 7×1×1 supercells, respectively. In comparison of total energies among differently sized supercells, we used the energy of the FM configuration as a reference. Among supercells in different sizes, the total energies of the FM configuration only differ in 0.08 meV/Ni, indicating a good energy convergence of our calculation. Each of those spiral magnetic orders was modeled using a certain propagation vector q within the first Brillouin zone in the framework of the generalized Bloch theorem (gBT) [18]. The Berry-phase approach [19] was adopted to derive the electrical polarization. Details of the calculations can be found in Supplemental Materials (Part S1).

The NiI₂ bulk crystal has a rhombohedral structure in space group $\bar{R}3m$ at room temperature (Fig. 1a), which is comprised of triangularly arranged Ni²⁺ cations ($3d^8$, $S=1$) and their coordinating I anions. In each Ni cation, eight d electrons fully occupy the three t_{2g} orbitals and half fill the two e_g orbitals, consistent with an averaged magnetic moment of 1.45 μ_B on each Ni atom. Our calculations revealed the fully relaxed lattice parameters of bulk NiI₂ in the experimentally observed spiral order are $a = 3.926$ Å, $b = 6.790$ Å and $c = 19.744$ Å (Figs. 1a and 1b), well consistent with the experimental values of $a = 3.919$ Å, $b = 6.765$ Å and $c = 19.635$ Å [20]. Bulk NiI₂ exhibits a spiral magnetic order (Spiral-B) with propagation vector $q_B = (0, 0.138, 1.457)$ (Figs. 1d and 1e) below $T_{N2}=59.5$ K [11,20]. Note that in the coordinates defined in the literature [11,20], $q_B = (0.138, 0, 1.457)$.

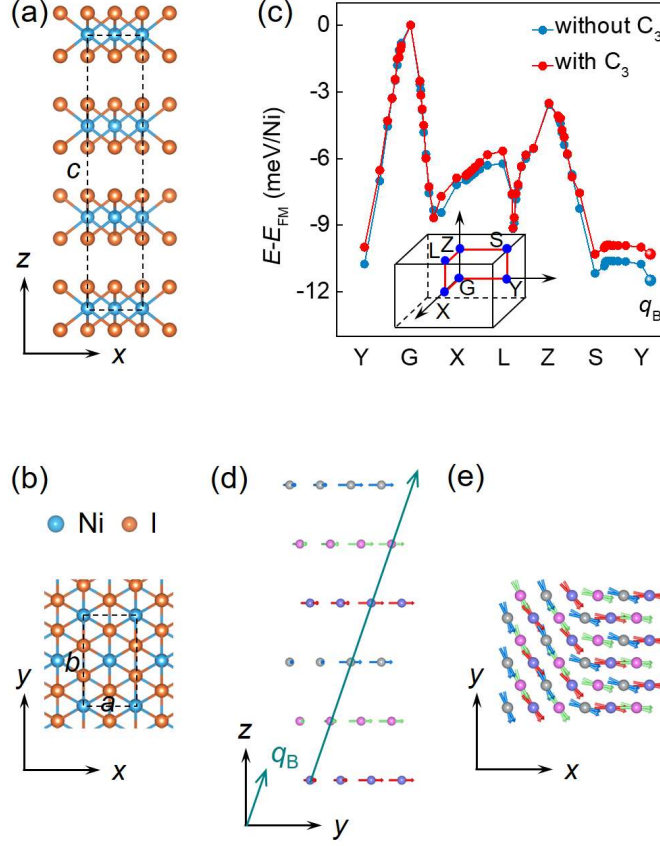


FIG. 1. Structural and magnetic groundstate of bulk NiI_2 . (a, b) Different perspectives of atomic structures of bulk NiI_2 . (c) Calculated energy difference between spiral orders with different q vectors and FM orders for bulk NiI_2 with and without C_3 structural rotation symmetry. The inset is considered q -path in the first Brillouin zone. The lowest energy locates at $q_B = (0, 0.138, 1.457)$, well consistent to the experimental observation [11]. (d-e) Schematic of the spin-spiral with $q_B = (0, 0.138, 1.457)$ in different views.

Our calculations well reproduced this magnetic groundstate of the bulk NiI_2 [11,21]. Particularly, we compared the total energy of Spiral-B with those of five collinear magnetic configurations shown in Fig. S1 and 55 other spiral configurations in different q values. Configuration Spiral-B shows the superior stability among all these configurations, regardless of the preservation of the C_3 symmetry, as listed in Table S1 and illustrated in Fig. 1c.-In addition, the found Spiral-B groundstate is robust in the presence of different on-site Coulomb interaction (U_{eff}) values (Fig. S2). We thus have confidence, in terms of reliability, of those results we predicted for the NiI_2 mono- and few-layers.

We considered 29 collinear magnetic orders and a 10×10 q -mesh for NiI_2 layers in thicknesses of ML to 5L to explore the layer-dependence of their magnetic groundstates. In the following discussion, we focus on the geometries showing (ML-C3) and not showing (ML-NC3) the C_3 symmetry for the monolayer because the geometric symmetry of the monolayer is more easily to be modulated by the substrate, as observed in previous studies [22,23]. While for thicker layers up to 5L, we concentrate on the constrain-free geometries as the substrate constrain rapidly relaxes in thicker layers [24-26].

The energy comparison of the q -mesh of the ML was illustrated in Figs. 2a and S3 for ML-C3 and ML-NC3, respectively. Both energy maps indicate a new energetically favored spiral configuration at $q_Y = (0, 0.5, 0)$ (Spiral-Y, Fig. 2b), which is propagating along the y direction in a $2\sqrt{3}a$ (across four Ni atoms along the zigzag chain) period. The Spiral-Y has comparable energetical stability with the AABB state, but is much more stable than other collinear and non-collinear magnetic configurations as listed in Table S2 and shown in Fig. S4. In particular, the AABB-AFM state is 0.05 meV/Ni more stable than Spiral-Y in the constrain-free geometry (ML-NC3) (inset in Fig. 2c). Constrain to maintain the ML-C3 structure slightly lifts up the energy of the ML, but largely favors the Spiral-Y configuration. For thicker NiI_2 layers from 2L up to 4L, Spiral-Y always shows the lowest energy among all considered configurations regardless of the geometric symmetry (Tables S3-S6 and Fig. S5), while the bulk groundstate Spiral-B restores at the thicknesses of 5L and maintains up to the bulk limit. All these results are summarized in a schematic magnetic phase diagram plotted in Fig. 2d.

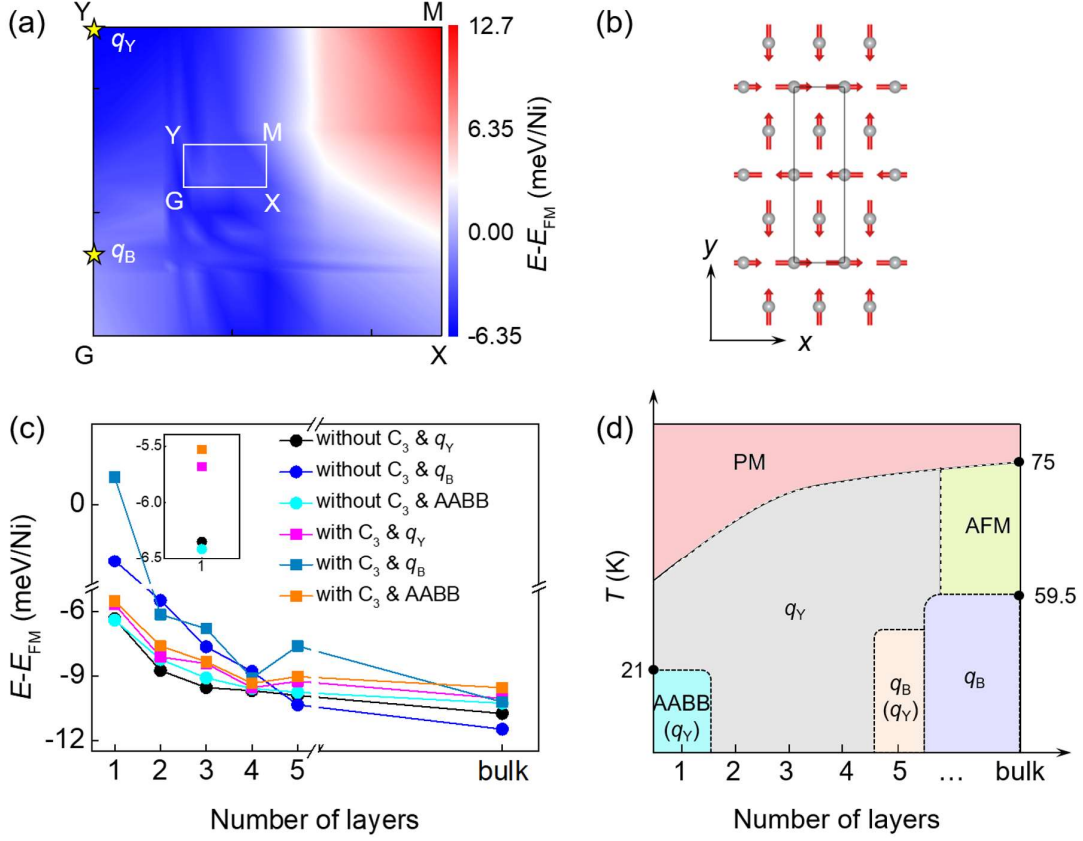


FIG. 2. Layer-dependent magnetic groundstate of NiI_2 . (a) 2D mapping of energy difference between spin-spiral and FM orders for ML NiI_2 without C_3 rotational symmetry. The inset is considered q -path in the first Brillouin zone. The spiral vectors in bulk NiI_2 (q_B) and Spiral-Y (q_Y) are labeled by the yellow stars. (b) Top view of the Spiral-Y. (c) Layer-dependent energy difference between spin-spiral and FM orders for both structures. The inset shows zoomed in energies for ML NiI_2 . (d) Schematic magnetic phase diagrams for different NiI_2 layers versus temperature. Those in the parentheses are for the structures with C_3 symmetry. PM and AFM represent paramagnetic and interlayer antiferromagnetic states. The transition temperatures for bulk and ML NiI_2 were adopted from the values reported in Ref. [11].

As the Spiral-Y and AABB-AFM orders show nearly identical energies in ML-NC3, we further examined the effective U value (U_{eff}) and functional dependences of their relative energies. The slightly more stable AABB-AFM state is robust in a U_{eff} range from 1.8 to 5.4 eV, as shown in Fig. S6a. The upper limit of this range, that is 5.4 eV, is substantially larger than the values used in the literature [27] and revealed by a linear response method [28]. This robustness was also double checked using different

functionals, namely, the PBE, PBE-D3, Revised PBE (RPBE), optB86b-vdW, and HSE06 hybrid functionals [29] with consideration of spin-orbit coupling (SOC), as illustrated in Fig. S6b.

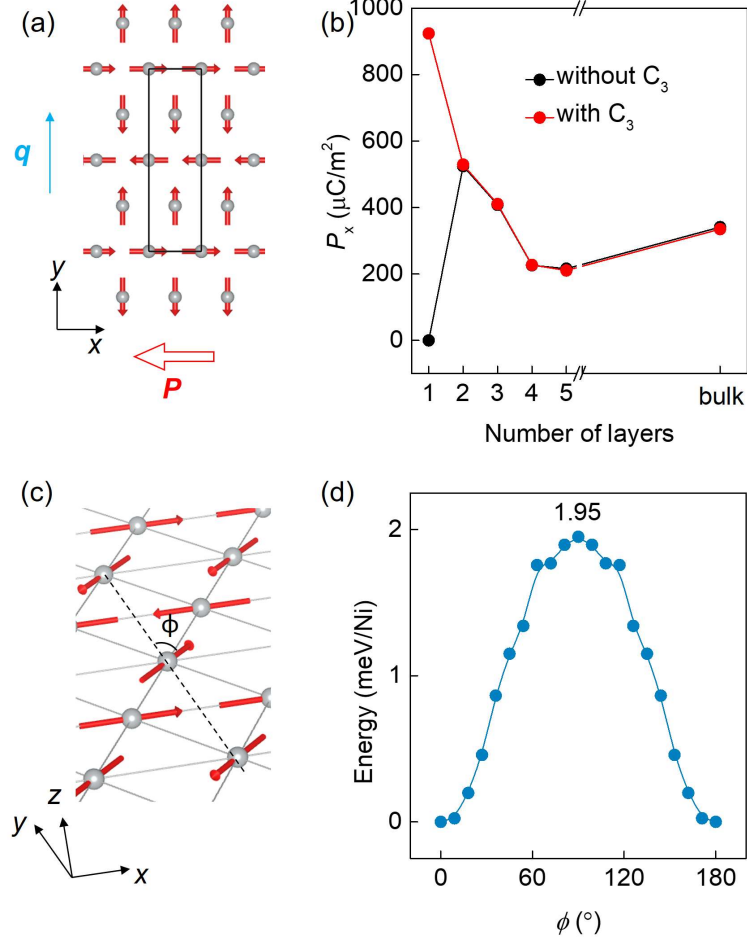


FIG. 3. Spin spiral induced ferroelectric polarization for NiI_2 . (a) Schematic plots for anticlockwise spin spiral in a $1 \times 2\sqrt{3}$ supercell (Spiral-Y) to generate in-plane electric polarizations parallel to the $-x$ direction. (c) Schematic diagram of spin canting process from the anticlockwise spin spiral to a clockwise spin spiral. (d) Calculated energy barrier for the spin canting process.

Spiral-Y is expected to induce electrical polarization in NiI_2 few layers through the inversed D-M interaction in form $P \parallel \hat{e} \times q$, where \hat{e} denotes the axis that the spiral spins rotate around [30]. As shown in Fig. 3a, the anticlockwise (clockwise) rotating Spiral-Y generates an in-plane electrical polarization in the $-x$ (x) direction (P_x),

which is consistent to the experimental observed electric polarization along the $-x$ direction in bulk NiI_2 [8]. The FM state, showing no electrical polarization, is used as the reference zero to show the layer-dependence of the electrical polarization in Fig. 3b. The NiI_2 bulk crystal shows an in-plane electric polarization vector parallel to the $-x$ direction with a value of $334.90 \mu\text{C}/\text{m}^2$, which is comparable to that of ML FeOCl ($\sim 390 \mu\text{C}/\text{m}^2$) [31], LiCu_2O_2 ($441.4 \mu\text{C}/\text{m}^2$) and LiCuVO_4 ($595.6 \mu\text{C}/\text{m}^2$) [32]. The value of P_x for the NiI_2 5L is, for some reason, slightly lower than that of the bulk, but it continuously increases from the 5L to 2L. However, the constrain-free monolayer undergoes a Spiral-Y to AABB-AFM transition at ML forming the ML-NC3 structure, which eliminates the total electrical polarization, while the ML-C3 structure exhibits $P_x = 923.74 \mu\text{C}/\text{m}^2$, ascribed to the Spiral-Y order. The ability of switching of polarization vectors characterizes a FE material rather than an electret. Figure 3c illustrates a likely spin canting process from the anticlockwise Spiral-Y configuration to the clockwise one, which has to surmount a switching energy barrier of $1.95 \text{ meV}/\text{Ni}$ (Fig. 3d).

Although the AABB-AFM configuration has no net electrical polarization, it shows an intralayer antiferroelectricity in the ML-NC3 structure which has a shortened lattice b relative to that of the FM order in ML-C3 (Table S5 and Fig. S7a). Displacements of Ni atoms in the AABB-AFM order are plotted in Fig. S7b, in which the Ni atoms in the same AFM stripe move to the opposite directions ($+y$ and $-y$) of 0.004 \AA , corresponding to a dipole moment of $\pm 4.84 \times 10^3 \mu\text{C}/\text{m}^2$ (Fig. S7c). As shown in Fig. S7d, the switching barrier between the two AFE phases is 5.63 meV , comparable to that of 3.76 meV for ferroelectric ML SnSe [33].

In short, there are three multiferroic phases competing in NiI_2 , including the newly found Spiral-Y + FE and the AABB-AFM + AFE states and the previously known Spiral-B + FE state. Thus, the NiI_2 monolayer is indeed a type-II multiferroic material at the 2D limit, but its multiferroicity is tunable between AFM+AFE and Spiral + FE by the in-plane geometric symmetry, which helps explain the “contradicting” experimental results reported in Refs. [10] and [11].

The NiI₂ ML was supported on a SiO₂ [10] and a *h*BN [11] substrate, respectively in those two experiments. We thus constructed a ML-NiI₂ 10×4√3 / ML-*h*BN 9√3×11-R30 rectangular supercell to model the NiI₂/*h*BN interface, which shows out-of-plane corrugation that the *z* coordinates of Ni atoms and both I sublayers do vary up to 0.06 Å (see Figs. S8a and S9). Nonuniform in-plane strains further breaks the inversion symmetry, as shown in Figs. S8c and S8d for the *x* and *y* strains. In addition, explicit interfacial charge transfer from the BN layer to the I layer, indicating an out-of-plane electric polarization (Figs. S8e and S8f). Therefore, deposition of ML NiI₂ on *h*BN simultaneously breaks the structural inversion symmetry of NiI₂, corresponding to the observable SHG signals above 20 K in Ref. [11].

These strong modifications from the *h*BN substrate to the NiI₂ ML indicate a strong interacting strength between them, which, most likely, enables the preservation of the C₃ symmetry of the NiI₂ ML, as the *h*BN substrate exhibits the C₃ symmetry. Given the likely maintained C₃ symmetry, the NiI₂ monolayer favors the Spiral-Y order. Thus, the SHG signal could be further enhanced by the additional in-plane electrical polarization induced by the non-collinear Spiral-Y order which is formed below 20 K. This temperature dependent enhancement well explains the enhanced SHG signal below 20 K [11]. The amorphous SiO₂ substrate is a well saturated substrate that usually exhibits weak interactions with its supporting monolayers [34]. Therefore, the NiI₂ ML placed on amorphous SiO₂ is nearly “constrain-free” and shows the AAB-B-AFM order, which preserves the inversion symmetry and thus showing no temperature dependent SHG enhancement [10].

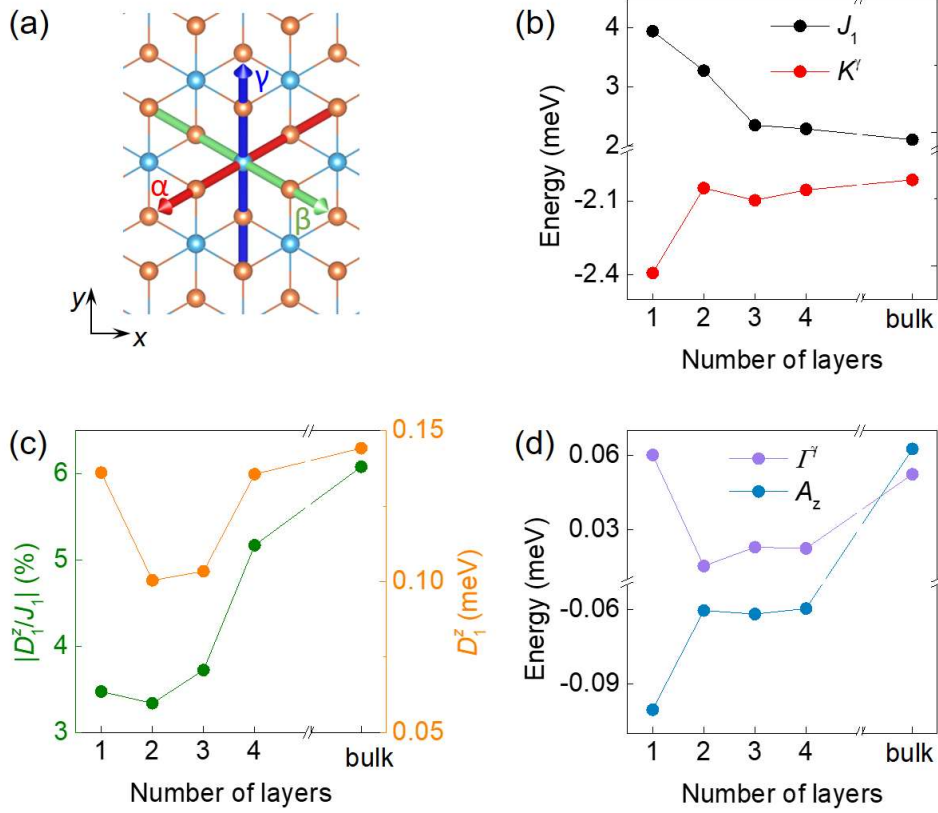


FIG. 4. Layer-dependent magnetic coefficients and MAE maps of NiI_2 without symmetry limitation. (a) Schematization of the Kitaev basis $\{\alpha\beta\gamma\}$ by red, green and blue arrows, respectively. (b-d) Evolution of J_1 , K^γ , $|D_1^Z/J_1|$, Γ^γ and A_z as a function of NiI_2 layers.

The remaining issue lies in the reason why NiI_2 hosts those three competing states. We thus plotted layer-dependent spin-exchange parameters for the nearest Heisenberg J_1 , Kitaev collinear K^γ and non-collinear Γ^γ (illustrated in Fig. 4a), D-M D_1^Z and single-ion anisotropy A_z for ML-C3 and ML-NC3 in Figs. 4b to 4d and S10b to S10c. The parallel J_1 is nearly unchanged as the thickness shrinks from the bulk (2.37 meV) to the 3L and then it rapidly increases in 2L (3.01 meV) and ML (3.92 meV), while the anti-parallel K^γ shares a similar trend that it keeps nearly constant down to 2L ($-2.01 \sim -2.05$ meV) and abruptly enlarges its absolute value to 2.39 meV at ML, as illustrated in Fig. 4b. Such rapidly strengthened J_1 and K^γ and slightly varied absolute value of D_1^Z (0.10 \sim 0.15 meV) effectively reduces the $|D_1^Z/J_1|$ ratio from roughly 6% to slightly over 3%.

It was usually believed that a system with the $|D/J|$ ratio larger than 5% could lead to a non-collinear magnetic order [35,36]. In addition, although the tilting I^γ shows it's the largest value (0.06 meV) at ML, the most negative A_z (-0.10 meV) competes with I^γ , keeping the moments in the x-y plane. It is interesting that both the parallel coupling J_1 and the anti-parallel coupling K^γ are simultaneously enhanced at ML. Their competitions lead the frustrated moments to rotate in the $(0, 0, \pi, \pi)$ period (AABB-AFM) or the $(\frac{\pi}{2}, \frac{\pi}{2}, \frac{\pi}{2}, \frac{\pi}{2})$ period (Spiral-Y) in the x-y plane, exhibiting the Spiral-B to Spiral-Y or AABB-AFM transition.

For few-layers from 2L to 4L, the fastest changing exchange strength lies in the $|D/J|$ ratio which rapidly increase from $\sim 3\%$ to over 5% (Fig. 4d), thus more favoring non-collinear orders and explains the eliminated collinear AABB-AFM order. While the non-collinear I^γ (0.02~0.03 meV) remain small and anisotropy A_z (-0.06 ~ -0.07 meV) is still negative in 2L to 4L (Fig. 4d), the non-collinear order is, although becoming favored, still confined in the x-y plane. At the bulk limit, the largest $|D/J|$ ratio (Fig. 4c) and the second largest I^γ (Fig. 4d) dominate, as other interactions like J_1 , K^γ and I^γ are the smallest. The $|D/J|$ ratio ensures non-collinear orders, the A_z changes to positive, and the I^γ interaction rotates the spiral plane from the x-y to the α - β plane [11], which differentiates Spiral-B and Spiral-Y.

In summary, we comprehensively exploited three multiferroic phases of NiI₂ from the bulk to the monolayer limit. The magnetic groundstates of bulk to 2L NiI₂ vary from the spiral orders with the propagation vectors of $q_B=(0, 0.138, 1.457)$ and $q_Y=(0, 0.5, 0)$ depending on the structural symmetry. Such non-collinear magnetic orders can induce in-plane electric polarization. Monolayer NiI₂ is a type-II multiferroic material with its multiferroicity tunable between AABB-AFM+AFE and Spiral-Y+FE depending on the structural symmetry. The transition of magnetic groundstates from bulk to ML NiI₂ is due to the competition between the layer-dependent Heisenberg isotropic exchange, D-M interaction, Kitaev, and single-ion anisotropy. Our theoretical results not only deepen

the understanding of the multiferroic properties from bulk to ML NiI₂, but also provide meaningful guidance for exploring vdW multiferroics down to 2D limit.

Acknowledgment

We gratefully acknowledge the National Natural Science Foundation of China (Grants No. 11974422 and 12204534). W.J. gratefully acknowledges financial support from the Ministry of Science and Technology (MOST) of China (Grant No. 2018YFE0202700), the Strategic Priority Research Program of Chinese Academy of Sciences (Grant No. XDB30000000), the Fundamental Research Funds for the Central Universities, and the Research Funds of Renmin University of China [Grants No. 22XNKJ30]. N.L. was supported by the China Postdoctoral Science Foundation (2022M713447). Calculations were performed at the Physics Lab of High-Performance Computing of Renmin University of China and Shanghai Supercomputer Center.

References

- [1] N. A. Spaldin and R. Ramesh, *Nat Mater* **18**, 203 (2019).
- [2] T. Kimura, T. Goto, H. Shintani, K. Ishizaka, T. Arima, and Y. Tokura, *Nature* **426**, 55 (2003).
- [3] N. Terada *et al.*, *Phys. Rev. Lett.* **129**, 217601 (2022).
- [4] N. A. Spaldin, *Nature Reviews Materials* **2**, 17017 (2017).
- [5] M. Fiebig, T. Lottermoser, D. Meier, and M. Trassin, *Nature Reviews Materials* **1**, 16046 (2016).
- [6] S. Dong, H. Xiang, and E. Dagotto, *Natl Sci Rev* **6**, 629 (2019).
- [7] S. Dong, J.-M. Liu, S.-W. Cheong, and Z. Ren, *Advances in Physics* **64**, 519 (2015).
- [8] T. Kurumaji, S. Seki, S. Ishiwata, H. Murakawa, Y. Kaneko, and Y. Tokura, *Phys. Rev. B* **87**, 014429 (2013).
- [9] H. Liu *et al.*, *ACS Nano* **14**, 10544 (2020).
- [10] H. Ju *et al.*, *Nano Lett.* **21**, 5126 (2021).
- [11] Q. Song *et al.*, *Nature* **602**, 601 (2022).
- [12] A. S. Botana and M. R. Norman, *Phys. Rev. Mater.* **3**, 044001 (2019).
- [13] M. Lu, Q. Yao, C. Xiao, C. Huang, and E. Kan, *ACS Omega* **4**, 5714 (2019).
- [14] V. V. Kulish and W. Huang, *J. Mater. Chem. C* **5**, 8734 (2017).
- [15] J. Y. Ni, X. Y. Li, D. Amoroso, X. He, J. S. Feng, E. J. Kan, S. Picozzi, and H. J. Xiang, *Phys. Rev. Lett.* **127**, 247204 (2021).
- [16] J. P. Perdew, K. Burke, and M. Ernzerhof, *Phys. Rev. Lett.* **77**, 3865 (1996).
- [17] S. Grimme, J. Antony, S. Ehrlich, and H. Krieg, *The Journal of Chemical Physics* **132**, 154104 (2010).
- [18] L. M. Sandratskii, *Advances in Physics* **47**, 91 (1998).
- [19] R. D. Kingsmith and D. Vanderbilt, *Phys. Rev. B* **47**, 1651 (1993).
- [20] S. R. Kuindersma, J. P. Sanchez, and C. Haas, *Physica B & C* **111**, 231 (1981).
- [21] H. Ju *et al.*, *Nano Lett.* **21**, 5126 (2021).
- [22] Z. Zhu *et al.*, *Phys. Rev. Lett.* **119**, 106101 (2017).
- [23] S. Paul, R. Torsi, J. A. Robinson, and K. Momeni, *ACS Appl Mater Interfaces* **14**, 18835 (2022).
- [24] Q. Li, C. Lee, R. W. Carpick, and J. Hone, *physica status solidi (b)* **247**, 2909 (2010).
- [25] K. Kang, K. H. Lee, Y. Han, H. Gao, S. Xie, D. A. Muller, and J. Park, *Nature* **550**, 229 (2017).
- [26] B. Li *et al.*, *Nature Materials* **20**, 818 (2021).
- [27] Q. Cui, J. Liang, B. Yang, Z. Wang, P. Li, P. Cui, and H. Yang, *Phys. Rev. B* **101**, 214439 (2020).
- [28] M. Cococcioni and S. de Gironcoli, *Phys. Rev. B* **71**, 035105 (2005).
- [29] J. Paier, M. Marsman, K. Hummer, G. Kresse, I. C. Gerber, and J. G. Ángyán, *The Journal of chemical physics* **124**, 154709 (2006).
- [30] S. W. Cheong and M. Mostovoy, *Nature Materials* **6**, 13 (2007).
- [31] D. L. Bao, A. O'Hara, S. Du, and S. T. Pantelides, *Nano Lett.* **22**, 3598 (2022).
- [32] H. J. Xiang and M. H. Whangbo, *Phys. Rev. Lett.* **99**, 257203 (2007).
- [33] R. X. Fei, W. Kang, and L. Yang, *Phys. Rev. Lett.* **117** (2016).
- [34] L. Su, Y. Yu, L. Cao, and Y. Zhang, *Nano Res* **8**, 2686 (2015).

[35] Y. L. Ga, Q. R. Cui, Y. M. Zhu, D. X. Yu, L. M. Wang, J. H. Liang, and H. X. Yang, *Npj Comput Mater* **8**, 128 (2022).

[36] C. S. Xu, J. S. Feng, S. Prokhorenko, Y. Nahas, H. J. Xiang, and L. Bellaiche, *Phys. Rev. B* **101**, 060404(R) (2020).

Supporting Information

Varied Competition among Three Multiferroic Phases of NiI₂ from the Bulk to the Monolayer Limit

Nanshu Liu¹, Cong Wang¹, Changlin Yan¹, Jun Hu^{2*}, Yanning Zhang^{3*}, Wei Ji^{1*}

¹*Beijing Key Laboratory of Optoelectronic Functional Materials & Micro-Nano Devices,*

Department of Physics,

Renmin University of China, Beijing 100872, China

²*School of Physical Science and Technology, Ningbo University, Ningbo, 315211, China*

³*Institute of Fundamental and Frontier Sciences, University of Electronic Science and Technology
of China, Chengdu, 610054, China*

S1. Methods

Density functional theory (DFT) calculations were performed using the generalized gradient approximation (GGA) for the exchange-correlation potential, the projector augmented wave (PAW) method [1,2], and a plane-wave basis set as implemented in the Vienna *ab initio* simulation package (VASP) [3,4]. A sufficient vacuum layer over 20 Å along the z direction was adopted to eliminate interactions among image layers. Spin-orbit coupling (SOC) was considered in all total energy calculations. The on-site Coulomb interaction was considered with a U value of 4.2 eV and a J value of 0.8 eV for Ni 3d orbitals according to the literatures [5,6] and our energy test calculations of four collinear (CL) and a non-collinear (NCL) magnetic configurations (Fig. S1). The Berry phase method [7] was adopted to evaluate the spiral magnetic order induced electric polarization. The transition barrier for monolayer (ML) NiI₂ from the in-plane antiferroelectric (AFE) phase of AABF-AFM order to a non-electric phase with C_3 symmetry was calculated using the climbing image nudged elastic band (CINEB) method [8]. All atoms, lattice volumes and shapes in each supercell were allowed to relax until the residual force on each atom was less than 0.01 eV/Å. Grimme's semiempirical D3 scheme [9] for dispersion correction was employed to describe the vdW interactions in combination with the Perdew-Burke-Ernzerhof functional (PBE-D3) [10]. This combination was found to be capable of offering comparable accuracy, but at a less computational cost, to the optB86b-vdW functional for describing geometric properties of layered materials [11].

Spin-exchange coupling (SEC) parameters were extracted based on a Heisenberg Hamiltonian below [12],

$$H = -\frac{1}{2} \left[\sum_{i,j;x,y,z} J_{ij} \mathbf{S}_i \cdot \mathbf{S}_j + \sum_{i,j;\alpha,\beta(\gamma)} \left(K_{ij} S_i^\gamma S_j^\gamma + \Gamma_{ij} (S_i^\alpha S_j^\beta + S_i^\beta S_j^\alpha) \right) + \sum_{i,j;x,y,z} D_{ij} \mathbf{S}_i \times \mathbf{S}_j + 2 \sum_{i;x,y,z} A_z \mathbf{S}_i^2 \right]$$

$$\begin{aligned}
&= -\frac{1}{2} \left[\sum_{i,j} J_{ij} \mathbf{S}_i \cdot \mathbf{S}_j + \sum_{i,j} \left(K_{ij}^\gamma S_i^\gamma S_j^\gamma + \Gamma_{ij}^\gamma (S_i^\alpha S_j^\beta + S_i^\beta S_j^\alpha) \right) \right. \\
&\quad \left. + \sum_{i,j;x,y,z} D_{ij} \mathbf{S}_i \times \mathbf{S}_j + 2 \sum_i A_z S_z^2 \right]
\end{aligned} \tag{S1}$$

Here, A_z represents the single-ion anisotropy parameter, J is the isotropic exchange parameter, D is the Dzyaloshinskii-Moriya (D-M) interaction parameter, K_{ij}^γ and Γ_{ij}^γ are so-called Kitaev interaction parameters [13] (labeled in Fig. 4a in main text), respectively.

To calculate the layer-dependent D-M interaction parameter D_{12}^x , we considered the following four spin configurations in which the spins 1 and 2 are oriented along the y and z axes, respectively: (i) $\mathbf{S}_1 = (0, S, 0)$, $\mathbf{S}_2 = (0, 0, S)$, (ii) $\mathbf{S}_1 = (0, S, 0)$, $\mathbf{S}_2 = (0, 0, -S)$, (iii) $\mathbf{S}_1 = (0, -S, 0)$, $\mathbf{S}_2 = (0, 0, S)$, (iv) $\mathbf{S}_1 = (0, -S, 0)$, $\mathbf{S}_2 = (0, 0, -S)$ [14]. In these four spin orders, the spins of all the other spin sites are the same and are along the x direction. The spin interaction energy for the four spin configurations can be written as:

$$\begin{aligned}
E_1 &= S_1^y D_{12}^x S_2^z - S_1^y \sum_{j \neq 1,2} D_{1j}^z S_j^x + S_2^z \sum_{i \neq 1,2} D_{i2}^y S_i^x + E_{other} \\
E_2 &= -S_1^y D_{12}^x S_2^z - S_1^y \sum_{j \neq 1,2} D_{1j}^z S_j^x - S_2^z \sum_{i \neq 1,2} D_{i2}^y S_i^x + E_{other} \\
E_3 &= -S_1^y D_{12}^x S_2^z + S_1^y \sum_{j \neq 1,2} D_{1j}^z S_j^x + S_2^z \sum_{i \neq 1,2} D_{i2}^y S_i^x + E_{other} \\
E_4 &= S_1^y D_{12}^x S_2^z + S_1^y \sum_{j \neq 1,2} D_{1j}^z S_j^x - S_2^z \sum_{i \neq 1,2} D_{i2}^y S_i^x + E_{other}
\end{aligned} \tag{S2}$$

Therefore, the D_{12}^x is:

$$D_{12}^x = \frac{1}{4S^2} (E_1 + E_4 - E_2 - E_3) \tag{S3}$$

The D-M parameters for the y and z directions were calculated by the same method.

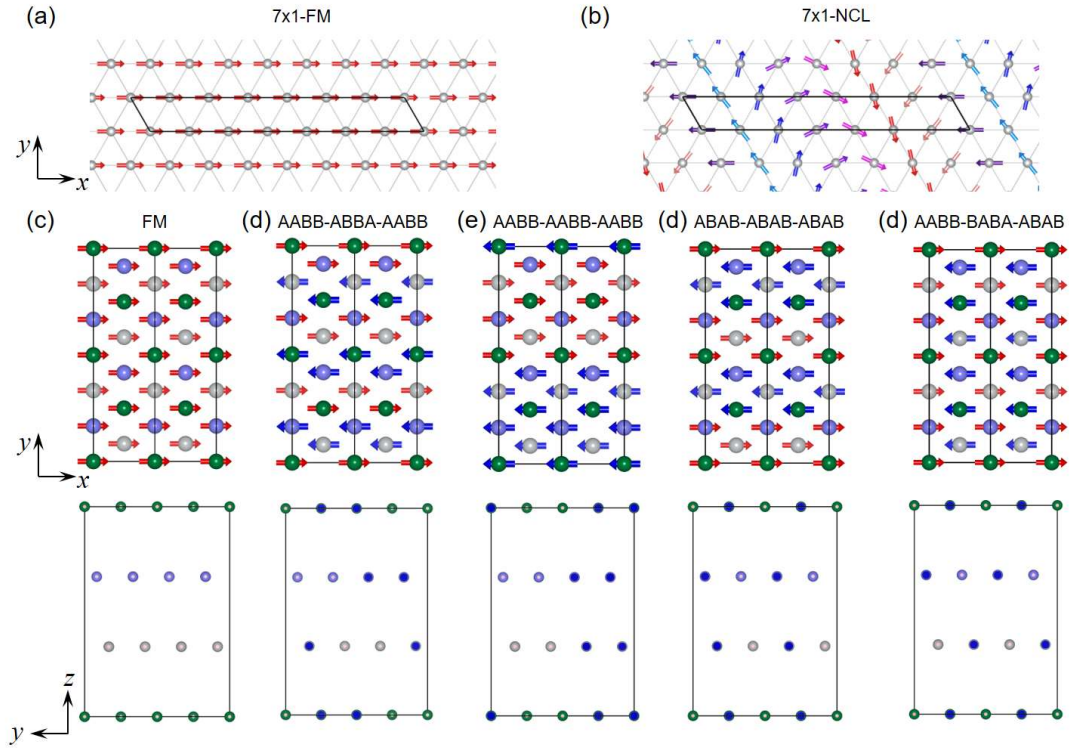


FIG. S1. Collinear and non-collinear magnetic configurations for bulk NiI_2 considered in this work. Black boxes represent the different supercells. The spin directions are labeled by arrows.

Table S1 Total energies of bulk NiI₂ with collinear and non-collinear (NCL) magnetic configurations (labeled in Fig. S1) relative to that of ferromagnetic (FM) order. The values in the parentheses are relative energies with C₃ rotational symmetry. $m \times n$ indicates number of supercells along a and b directions.

Lattice	Mag. Config.	ΔE (meV/Ni)
1×1	FM	0
7×1	FM	0.08
	$q = (0.143, 0, 0)$	-6.54
1×√3	$q_Y = (0, 0.5, 0)$	-10.75 (-10.17)
	$q = (0, 0.5, 0.5)$	-11.17 (-10.21)
	$q_B = (0, 0.138, 1.457)$	-11.48 (-10.30)
1×2√3	AABB-BAAB-BBAA	-10.01 (-9.73)
	AABB-AABB-AABB	-9.74 (9.62)
	ABAB-ABAB-ABAB	6.89 (6.71)
	ABAB-BABA-ABAB	11.76 (11.38)

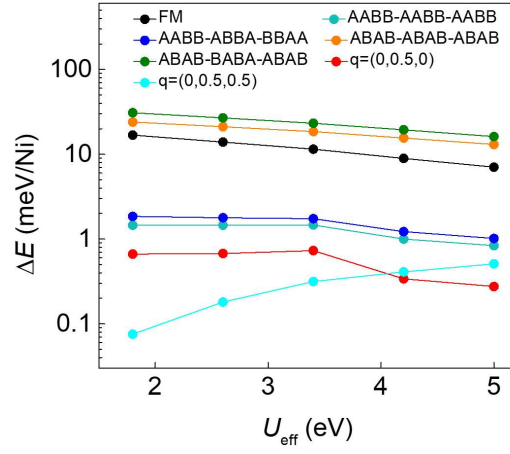


FIG. S2. Comparison of total energies of different magnetic orders to that of spiral spin $q_B = (0, 0.138, 1.457)$ for bulk NiI_2 as a function of effective on-site U values.

Table S2 Total energies of ML NiI₂ with collinear and NCL magnetic configurations (labeled in Fig. S3) relative to that of ferromagnetic order. $m \times n$ indicates number of supercells along a and b directions.

Lattice	Mag. Config.	ΔE (meV/Ni)
1×1	FM	-0.50
7×1	FM	-0.55
	$q = (0.143, 0, 0)$	-4.93
3×2	FM	-0.54
	NCL	10.62
3×3	FM	-0.55
	NCL	3.74
$\sqrt{3} \times \sqrt{3}$	FM	-0.07
	NCL	4.21
$2\sqrt{3} \times \sqrt{3}$	FM	-0.09
	NCL	-0.51
$2 \times 2\sqrt{3}$	FM	0.53
	AABB	-5.73
	ABAB	15.09
	ZZ	2.77
1× $\sqrt{3}$	FM	0
	$q_Y = (0, 0.5, 0)$	-5.68
	$q_B = (0, 0.138, 1.457)$	0.68

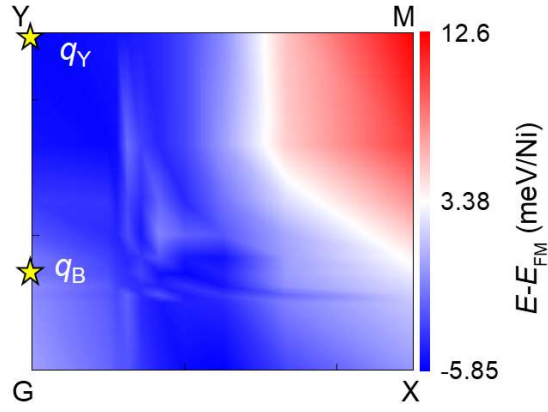


FIG. S3. Two-dimensional (2D) mapping of energy difference between spin-spiral and FM orders for ML NiI₂ with C₃ rotational symmetry. The spiral vectors in bulk NiI₂ (q_B) and Spiral-Y (q_Y) are labeled by the yellow stars.

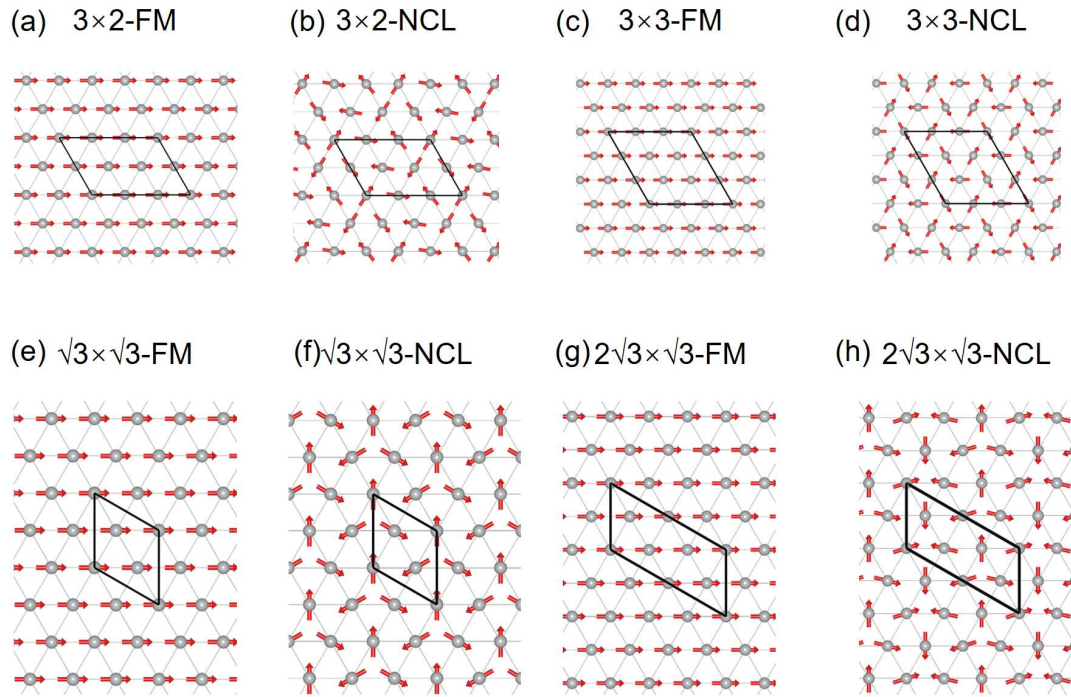


FIG. S4. Collinear and non-collinear magnetic configurations for ML NiI₂ considered in this work. Black boxes represent the different supercells. The spin directions are labeled by red arrows.

Table S3 Relative energies of different magnetic configurations to that of FM state for bilayer (2L) NiI₂ with constrain-free symmetry, which are labeled in Fig. S4. The values in parentheses are for those with symmetry-limitation. $m \times n$ indicates number of supercells along a and b directions.

Lattice	Mag. Config.	ΔE (meV/Ni)
	FM	0 (-0.36)
$1 \times 2\sqrt{3}$	AABB-AABB	-8.23 (-7.96)
	AABB-ABBA	-7.57 (-7.50)
	$q=(0.143, 0, 0)$	-3.52
$1 \times \sqrt{3}$	$q_Y=(0, 0.5, 0)$	-8.75 (-8.48)
	$q_B=(0, 0.138, 1.457)$	-5.50 (-6.50)

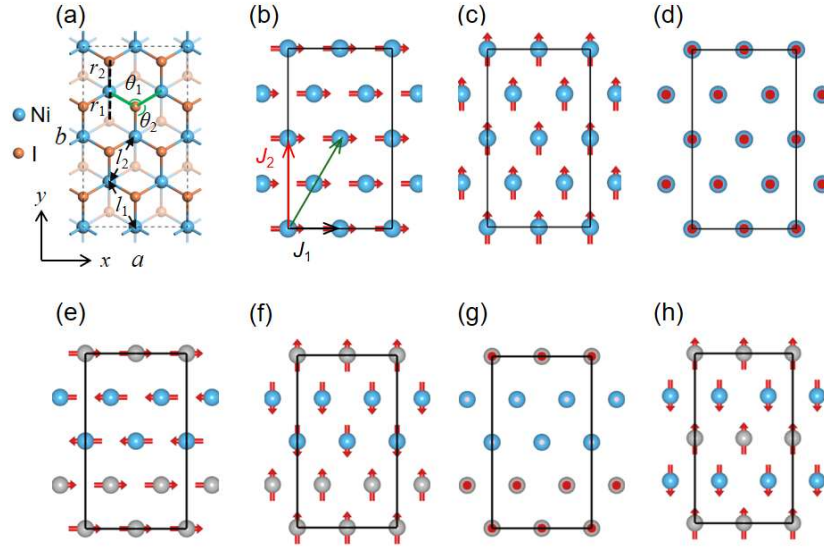


FIG. S5. (a) Top view of ML NiI₂. Black rectangle labels the $2 \times 2\sqrt{3}$ supercell. The blue and orange balls indicate Ni and I atoms. Several key structural parameters (including r_1 , r_2 , θ_1 , θ_2 , l_1 and l_2) are marked. Different collinear spin configurations along x , y , and z directions, including (b) ferromagnetic (FM) order along the x direction (FM _{x}), (c) FM _{y} , (d) FM _{z} , (e) AABB-anti-ferromagnetic order along the x direction (AABB-AFM _{x}), (f) AABB-AFM _{y} , (g) AABB-AFM _{z} . and (h) ABAB-AFM _{y} .

Table S4 Relative energies of different magnetic configurations to that of FM state for 3L NiI₂ with constrain-free symmetry. The values in parentheses are for those with symmetry-limitation. $m \times n$ indicates number of supercells along a and b directions.

Lattice	Mag. Config.	ΔE (meV/Ni)
	FM	0 (-0.49)
$1 \times 2\sqrt{3}$	AABB-AABB-AABB	-9.10 (-8.83)
	AABB-ABBA-BBAA	-8.30 (-8.20)
	ABAB-ABAB-ABAB	2.62 (2.35)
	ABAB-BABA-ABAB	4.96 (4.65)
$1 \times \sqrt{3}$	$q_Y=(0, 0.5, 0)$	-9.55 (-8.92)
	$q_B=(0, 0.138, 1.457)$	-7.65 (-7.30)

Table S5 Relative energies of different magnetic configurations to that of FM state for 4L NiI₂ with constrain-free symmetry. The values in parentheses are for those with symmetry-limitation. $m \times n$ indicates number of supercells along a and b directions.

Lattice	Mag. Config.	ΔE (meV/Ni)
	FM	0 (-0.52)
$1 \times 2\sqrt{3}$	AABB-AABB-AABB-AABB	-9.58 (-9.35)
	AABB-AABB-ABBA-ABBA	-9.10 (-9.10)
	AABB-ABBA-ABBA-AABB	-9.23 (-9.25)
	AABB-AABB-AABB-ABBA	-9.70 (-9.51)
	ABBA-ABBA-ABBA-AABB	-9.70 (-9.51)
$1 \times \sqrt{3}$	$q_Y=(0, 0.5, 0)$	-9.71 (-9.55)
	$q_B=(0, 0.138, 1.457)$	-8.79 (-9.10)

Table S6 Relative energies of different magnetic configurations to that of FM state for 5L NiI₂ with constrain-free symmetry. The values in parentheses are for those with symmetry-limitation. $m \times n$ indicates number of supercells along a and b directions.

Lattice	Mag. Config.	ΔE (meV/Ni)
	FM	0 (-0.53)
$1 \times 2\sqrt{3}$	AABB-AABB-AABB-AABB-AABB	-9.80 (-9.60)
	AABB-AABB-ABBA-AABB-AABB	-9.64 (-9.53)
	AABB-ABBA-AABB-ABBA-AABB	-9.30 (-9.35)
	ABAB-ABAB-ABAB-ABAB-ABAB	4.85 (4.46)
	AABB-AABB-AABB-ABBA-ABBA	-4.87 (-5.12)
	ABBA-ABBA-ABBA-AABB-AABB	-9.67 (-9.72)
$1 \times \sqrt{3}$	$q_Y=(0, 0.5, 0)$	-9.91 (-9.78)
	$q_B=(0, 0.138, 1.457)$	-10.35 (-8.15)

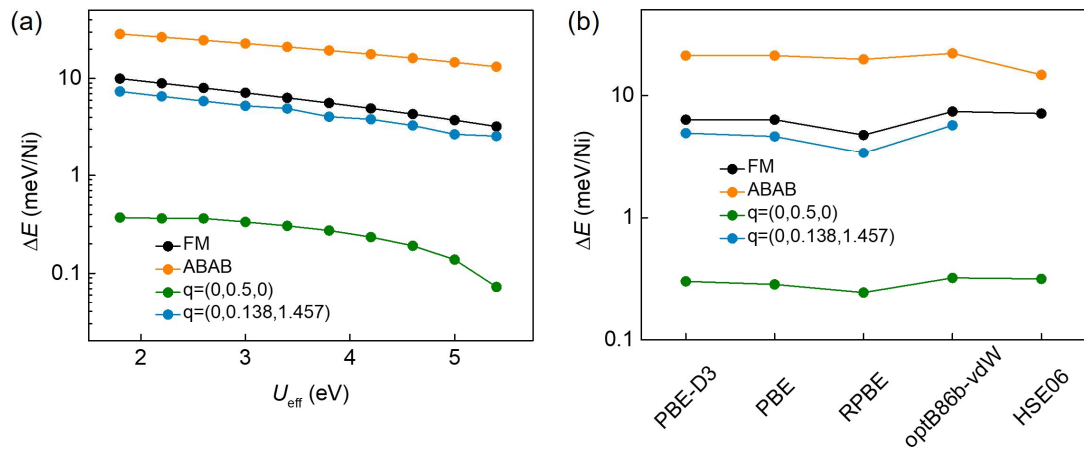


FIG. S6. Comparison of total energies of different magnetic orders to that of AABBAFM state for ML NiI_2 without symmetry limitation as a function of (a) effective on-site U values and (b) functionals. SOC effect is considered in PBE-D3, PBE, RPBE, HSE06 functionals.

Table S5 Structural and magnetic properties of monolayer NiI₂ with different spin configurations (marked in Fig. S4). Sym. represents the space point.

spin config.	a (Å)	b (Å)	l_1 (Å)	l_2 (Å)	θ_1 (°)	θ_2 (°)	Sym.	ΔE (meV/Ni)
FM	7.86	13.61	3.93	3.93	91.21	91.21	$P\bar{3}m1$	6.02
AABB-AFM	7.85	13.58	3.91	3.93	90.98	91.15	$P21/m$	0.0
ABAB-AFM	7.86	13.61	3.93	3.93	91.18	91.18	$P21/m$	20.73
ZZ-AFM	7.87	13.63	3.91	3.93	90.95	91.13	$P2/C$	8.41

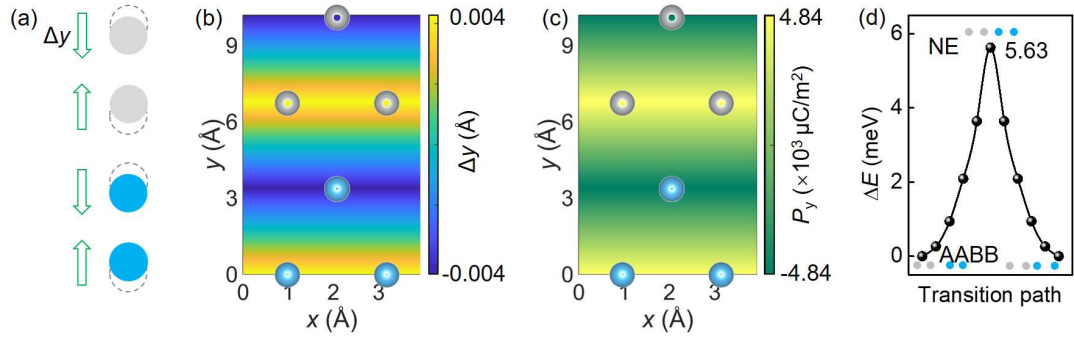


FIG. S7. Intralayer antiferroelectric (AFE) properties of freestanding ML NiI₂ with the AABB-AFM structure. (a) Schematic plot of displacements of Ni atoms along the y direction relative to the FM one. (b) Displacement of Ni atoms in AABB-AFM configuration along y direction. (c) Electric polarization of Ni atoms along the y direction in the AABB-AFM state calculated by the Berry phase method. (f) Transition pathway for ML NiI₂ between the two AFE phases through a non-electric (NE) phase. The number is the transition barrier (in meV). The blue and gray circles represent the Ni atoms in different stripes, respectively.

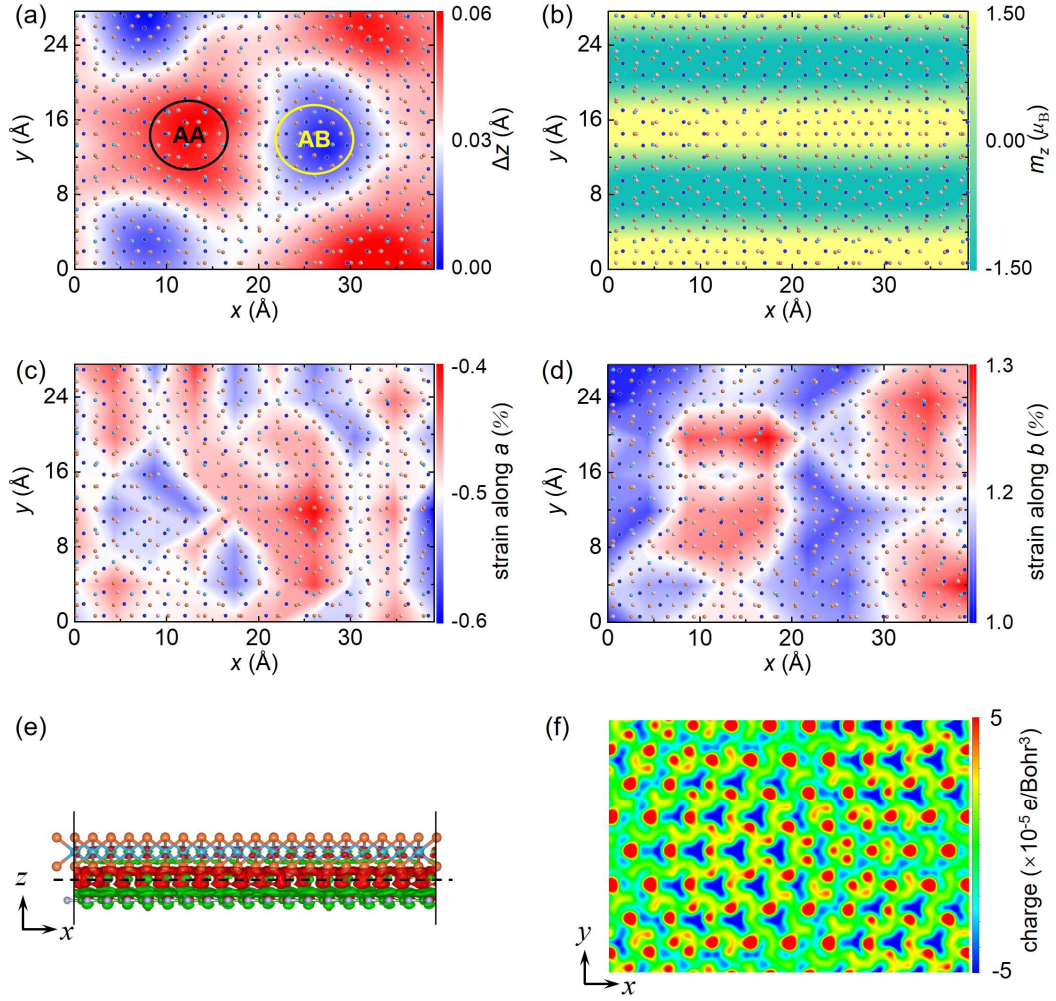


FIG. S8. Structure and magnetism of the epitaxial ML NiI_2 on $h\text{BN}$, including (a) mapping of the variation of z coordinates and (b) magnetic moments of Ni atoms in the heterostructure with the AABF-AFM state, in-plane strain along (c) a and (d) b directions, and (e) differential charge density and (f) 2D profile maps along the dashed lines labeled in (e) with an isosurface value of $5 \times 10^{-5} e/\text{Bohr}^3$. Red and blue contours are charge accumulation and depletion, respectively.

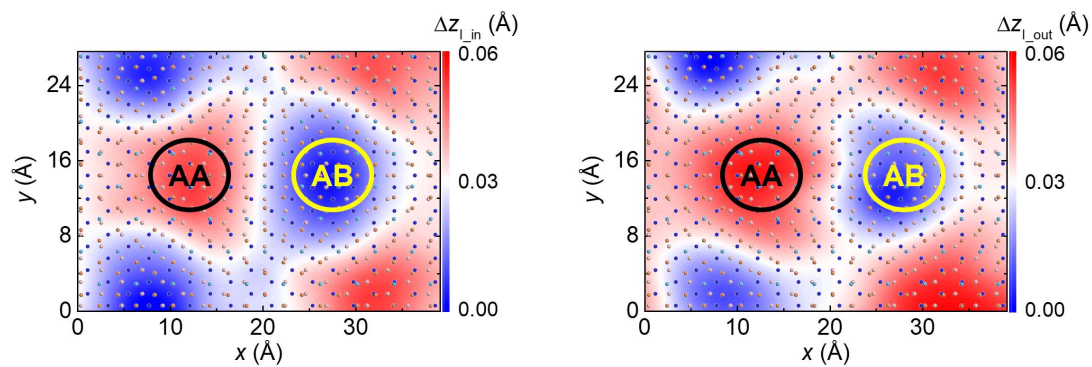


FIG. S9. Z coordinates mapping of the lower (I_{in}) and upper (I_{out}) I atoms of ML NiI_2 on hBN .

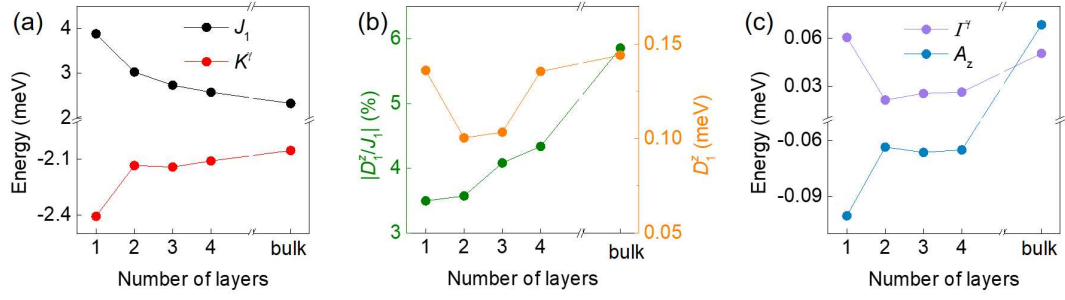


FIG. S10. Layer-dependent magnetic coefficients and MAE maps of NiI₂ with symmetry limitation. (a-c) Evolution of J_1 , K^y , $|D_1^z/J_1|$, Γ^y and A_z as a function of NiI₂ layers.

Table S6 Isotropic exchange parameters J_1 , J_2 , J_3 for the nearest, second nearest, and third nearest Ni atoms of NiL₂ with and without symmetry limitation, respectively.

	constrained			constratin-free		
	J_1 (meV)	J_2 (meV)	J_3 (meV)	J_1 (meV)	J_2 (meV)	J_3 (meV)
ML	3.89	-0.24	-3.08	3.92	-0.26	-3.20
2L	3.03	-0.59	-2.82	3.01	-0.61	-2.94
3L	2.74	-0.72	-2.73	2.78	-0.80	-2.87
4L	2.58	-0.79	-2.71	2.62	-0.87	-2.84
bulk	2.33	-0.60	-2.95	2.37	-0.68	-3.08

References

- [1] P. E. Blöchl, Physical review B **50**, 17953 (1994).
- [2] G. Kresse and D. Joubert, Physical review b **59**, 1758 (1999).
- [3] G. Kresse and J. Furthmüller, Physical review B **54**, 11169 (1996).
- [4] G. Kresse and J. Furthmüller, Computational materials science **6**, 15 (1996).
- [5] I. Solovyev, P. Dederichs, and V. Anisimov, Physical Review B **50**, 16861 (1994).
- [6] A. S. Botana and M. R. Norman, Physical Review Materials **3**, 044001 (2019).
- [7] X. Gonze and C. Lee, Phys. Rev. B **55**, 10355 (1997).
- [8] G. Henkelman, B. P. Uberuaga, and H. Jónsson, The Journal of Chemical Physics **113**, 9901 (2000).
- [9] S. Grimme, Journal of computational chemistry **27**, 1787 (2006).
- [10] J. P. Perdew, K. Burke, and M. Ernzerhof, Physical review letters **77**, 3865 (1996).
- [11] L. Shulenburger, A. D. Baczewski, Z. Zhu, J. Guan, and D. Tomanek, Nano Lett. **15**, 8170 (2015).
- [12] J. L. Lado and J. Fernandez-Rossier, 2D Materials **4**, 035002 (2017).
- [13] C. S. Xu, J. S. Feng, H. J. Xiang, and L. Bellaiche, Npj Comput Mater **4**, 57 (2018).
- [14] H. J. Xiang, E. J. Kan, S.-H. Wei, M. H. Whangbo, and X. G. Gong, Phys. Rev. B **84**, 224429 (2011).